Shale Characterization Using Magnetic Resonance

Mohammad Sadegh Zamiri[1,2], *Jiangfeng* Guo[1,3], *Florea* Marica[1], *Laura* Romero-Zerón[2], and *Bruce J.* Balcom[1,*]

[1]UNB MRI Research Centre, Physics Department, University of New Brunswick, Fredericton, NB E3B 5A3, Canada
[2]Department of Chemical Engineering, University of New Brunswick, Fredericton, NB E3B 5A3, Canada
[3]State Key Laboratory of Petroleum Resources and Prospecting, China University of Petroleum (Beijing), Beijing, 102249, China

Abstract. Shale characterization while important is complicated by low porosity and low permeability. Nano-porosity and a high degree of heterogeneity present further difficulties. Magnetic resonance (MR) methods have great potential to provide quantitative and spatially resolved information on fluids present in porous rocks. The shale MR response, however, is challenging due to short-lived signals that deter quantitative signal detection and imaging. Multicomponent signals require high resolution methods for adequate signal differentiation. MR methods must cope with low measurement sensitivity at low field. In this paper, T_1-T_2^* and Look-Locker T_1^*-T_2^* methods were employed to resolve the shale signal for water, oil, and kerogen at high and low field. This permits fluid quantification and kerogen assessment. The T_1-T_2^* measurement was employed to understand and control contrast in the SPRITE imaging method. This permitted imaging that gave separate images of water and oil. Water absorption/desorption, evaporation, step pyrolysis, and water uptake experiments were monitored using T_1-T_2^* measurement and MR imaging. The results showed (1) the capability of the T_1-T_2^* measurement to differentiate and quantify kerogen, oil, and water in shales, (2) characterization of shale heterogeneity on the core plug scale, and (3) demonstrated the key role of wettability in determining the spatial distribution of water in shales.

1 Introduction

There are vast untapped hydrocarbon reserves in shale formations worldwide. Accurate rock characterization is essential for economic hydrocarbon production from such formations. Shale characterization includes, but is not limited to, quantification of pore-filling fluids, kerogen assessment, and understanding fluid storage and transport [1]. Shale fluid quantification methods are essential to estimate hydrocarbon reserves and to help guide reservoir and well development plans. Furthermore, kerogen, the solid organic matter in shale rocks, is commonly assessed due to a positive correlation between kerogen content in shales and reservoir quality [2]. Shale rocks commonly exhibit low porosity and permeability, nano-scale pores, and a high degree of heterogeneity which present challenges for characterization methods for such rocks. Conventional core analysis methods, such as retort, two-phase extraction, and Dean Stark method for fluid quantification, and pyrolysis and elemental analysis for kerogen assessment are cumbersome and sample destructive. They commonly rely on volumetric measurements which may be erroneous and provide no spatial information.

Shales exhibit a multiscale heterogeneity that controls fluid storage and transport [3-5]. These heterogeneities include laminated structure on millimetre and centimeter scale. On the micro-meter scale, inclusion of minerals and organic matter, and microfractures are evident. The shale pore network can only be detected at nanoscale. These features are commonly studied using imaging methods. However, available imaging methods [6-9], such as scanning electron microscopy (SEM) and nano-computed tomography (nano-CT), have limited field of view (FOV), are sample destructive, and are principally sensitive to the morphology and topology of the rock rather than the pore-filling fluids. Therefore, extensive computational methods are required not only to convert the spatial information to fluid flow and storage but also to upscale this information to accurately measure petrophysical quantities at a representative elementary volume (REV) [10].

Alternatively, ^1H magnetic resonance (MR) methods are non-destructive, robust, detect signal directly from fluid in nanopores of shale rocks, and provide images with centimeter scale FOV. MR methods rely on measurement of signal relaxation lifetimes (T_1, T_2, and T_2^*) and molecular diffusion. These variables are sensitive to molecular dynamics and molecular environment. MR methods for shale rocks present several challenges. (1) MR signal for shales is short-lived which hinders signal detection and quantification. (2) Several shale species such as brine, oil and kerogen contain hydrogen that gives rise to a multicomponent MR signal. (3) The short-lived signal prevents application of most MR imaging methods. (4) Current MR measurements are not compatible with instruments available for shale characterization. Most common MR scanners dedicated to rock core plug analysis operate at low field which provides a low sensitivity for shale measurements compared to high field measurements.

The best-known MR methods for shale characterization include T_1-T_2 relaxation correlation measurement [11-20] and Diffusion-T_2 measurement [15,19,20], commonly implemented at high field. These methods are limited by the echo time, often on the order of hundreds of microseconds, which is inadequate for resolving the fast-relaxing shale signal. This prevents quantitative signal detection and spatial encoding. Furthermore, shale signal peaks commonly overlap in relaxation correlation measurements which prevent signal

* Corresponding author: bjb@unb.ca

quantification. For example, at low field, the oil signal component overlaps with that of water [15,21]. Therefore, shale measurements are commonly performed at high field. To overcome the issue of signal overlap, it was proposed to (1) use the field dependency of oil to identify oil phase in shales [21], (2) use Diffusion-T_2 measurement to resolve oil and water signals at low field. However, the former requires special instrumentation, and the latter is only sensitive to free fluid in shale rocks [15].

In this paper, MR measurements on outcrop shale samples from Eagle Ford, Marcellus, and Barnett Formations are presented. 2D T_1-T_2^* relaxation correlation measurement [22,23] was introduced for shale characterization [24,25]. It was shown that the T_1-T_2^* technique can overcome some of the issues inherent in shale measurements by resolving the multicomponent shale signal and quantifying signal peaks at low and high field. The high resolution of the T_1-T_2^* method allows usage of a reference sample that helps produce consistent signal quantification between measurements. The T_1-T_2^* resolved signal was exploited in conjunction with water adsorption/desorption and evaporation experiments to quantify oil and water content in shale samples. A step pyrolysis measurement coupled with T_1-T_2^* measurement showed that the short transverse relaxation signal component was dominated by the kerogen content. Resolved kerogen signal was used to evaluate kerogen hydrocarbon generation potential. The Look-Locker T_1^*-T_2^* method [26], a variation of T_1-T_2^* technique, was used at low field to give quantitative water and oil content in shales, and kerogen assessment with high-sensitivity. The Look-Locker T_1^*-T_2^* technique permitted fast and quantitative shale measurement at low field. The centric-scan SPRITE imaging method [27,28] with magnetization preparation was employed to give 1D and 3D oil and water images on a core plug scale. The images acquired using this method showed that sample scale heterogeneities are commonly imposed by the shales' lamina. The natural water and oil distribution in shale samples was greatly influenced by the samples' bedding structure. Water uptake experiments were monitored using T_1-T_2^* measurement and the SPRITE imaging method with oil suppression. The results illustrated the wettability control of spatial water distribution in shales during spontaneous imbibition.

2 Theory

Molecules in liquids have fast tumbling motion through which the average magnetic perturbations caused by dipolar interactions vanishes. Therefore, these interactions are not responsible for relaxation in liquids. For solids, slow molecular motion results in residual dipolar interactions. Solid echo techniques can partially refocus these dephasing effects. In these techniques, large spin systems and molecular motion still lead to irreversible decay of the transverse magnetization [29].

The transverse magnetization decay is characterized by the spin-spin relaxation time, T_2. However, the primary time domain MR signal in this work is a free induction decay (FID), described by the effective spin-spin relaxation time, T_2^*. As a result of inhomogeneity in the magnetic field, transverse relaxation measured by the FID decays more rapidly than that solely due to only T_2 effects [30]. These field inhomogeneities can arise from (1) inhomogeneity in the underlying magnetic field, B_0 and (2) diamagnetic susceptibility mismatch between the sample's compositions, $\Delta\chi$. The effective spin-spin relaxation time, T_2^* is a combination of the spin-spin relaxation time, T_2 and the two inhomogeneity effects mentioned above and can be expressed using Eq. 1 [31].

$$\frac{1}{T_2^*} \approx \frac{1}{T_2} + \gamma \Delta B_0 + \gamma \Delta\chi B_0 \qquad (1)$$

where ΔB_0 is the breadth of the magnetic field distribution, B_0.

T_2 relaxation of liquids is commonly of the order hundreds of milliseconds whereas for solids such as kerogen in shales decay will occur in a few tens of microseconds. This prevents signal discrimination and quantification of fast-relaxing solid kerogen. In this regime, Eq. 1 for the T_2^* is dominated by the T_2 lifetime. Therefore, T_2^* contrast measured by FID can be used to estimate T_2 contrast. T_2^* can be measured with a greater accuracy compared to the T_2 lifetime in shales. Employment of T_2^* instead of T_2 in the 2D MR correlation measurements results in a better resolution of signal species.

3 Experimental section

3.1 Pulse sequences

3.1.1 2D relaxation correlation methods

T_1-T_2 relaxation correlation measurements were performed according to the pulse sequence shown in Figure 1a. The pulse sequence consists of two parts, a T_1 recovery stage and an acquisition part. During the saturation in the T_1 recovery stage, longitudinal magnetization is reduced to zero. This magnetization then partially recovers during the variable time τ_r. In the acquisition part, the signal is recorded using CPMG which collects data with an echo time, τ_e time spacing. The pulse sequence in Figure 1a is repeated with various τ_r values logarithmically spaced to cover the T_1 recovery of the sample magnetization.

T_1-T_2^* relaxation correlation measurements [22,23] were performed according to the pulse sequence shown in Figure 1b. The T_1 recovery stage is similar to that of T_1-T_2 measurement. In the acquisition part, the 90° pulse brings the recovered magnetization into the transverse plane to be detected in time by the FID with a short dwell time, dw, spacing between data points after a short deadtime, t_d. Multiple FIDs are acquired at various τ_r values logarithmically spaced to cover the T_1 recovery of the sample magnetization.

The pulse sequence for the Look-Locker T_1^*-T_2^* relaxation correlation measurement [26] is shown in Figure 1c. The effective longitudinal relaxation time, T_1^* is measured when a Look-Locker sequence is used. T_1^* is closely related to the T_1 relaxation time, according to Eq. 2a This measurement, by contrast to the T_1-T_2^* measurement, does not require performing various T_1 recoveries. Multiple FIDs are acquired by employing multiple low flip angle pulses, α during a single longitudinal magnetization recovery. These pulses are separated by a time τ. Therefore, T_1 recovery times

in this measurement are linearly spaced. A Look-Locker T_1^*-T_2^* measurement can be acquired substantially faster than a T_1-T_2^* measurement. Signal averaging can be performed to improve signal-to-noise ratio (SNR) and sensitivity of the measurement. This technique enables fast and quantitative measurements at low field. The signal intensities obtained using the Look-Locker T_1^*-T_2^* measurement should be corrected using Eq. 2b to give signal proportional to the hydrogen content [26].

$$\frac{1}{T_1^*} = \frac{1}{T_1} - \frac{\ln(\cos\alpha)}{\tau} \quad (2a)$$

$$S = \frac{S^*\tau}{(\tau + T_1^* \ln(\cos\alpha)).\sin\alpha} \quad (2b)$$

where S and S^* are signal proportional to the hydrogen content and signal obtained from Look-Locker T_1^*-T_2^* measurement, respectively. T_1^* is determined from the coordinate of the signal peak on the T_1^*-T_2^* correlation plot.

3.1.2 Imaging method

The imaging measurements were performed using the scheme presented in Figure 1d. The pulse sequence consists of a magnetization preparation stage and a readout part [32,33]. In the first part, the combination of 90° pulse and the spoiling gradient brings the longitudinal magnetization to zero. This magnetization partially recovers during the variable T_1 recovery time, τ_r. In the second part, the recovered magnetization is acquired using a centric-scan SPRITE readout. This gives the image signal according to Eq. 3.

$$S(r,\tau_r,t_p) = M_{\text{Prep}}(r,\tau_r).exp\left(-\frac{t_p}{T_2^*}\right).\sin\alpha \quad (3)$$

where M_{Prep} is a series of T_1-weighted images acquired for each τ_r, r is the position and t_p is the image encoding time. The FID decays for oil (red), water (blue), and kerogen (black) in shales are shown separately in Figure 1d for illustration purposes. The fast-decaying kerogen signal can be excluded from the image by choosing a long t_p. The t_p can be short enough to acquire oil and water signal. The prepared magnetization, M_{Prep} at each position is a superposition of all T_1 signal components recovered during τ_r. Therefore, M_{Prep} is described by the integral in Eq. 4 to give $\rho(r,T_1)$, the image signal resolved in the T_1 relaxation time.

$$M_{\text{Prep}}(r,\tau_r) = \int \rho(r,T_1).\left(1-\exp\left(-\frac{\tau_r}{T_1}\right)\right).dT_1 \quad (4)$$

3.2 Shale samples and experiments

Table 1 presents a summary of experiments performed on various shale samples at different magnetic fields. Shale samples were outcrop, provided by Kocurek Industries Inc. (Caldwell, TX), and were cylindrical in shape. Shale samples from the Eagle Ford Formation, the Marcellus Formation, and the Barnett Formation are referred to as EG, M, and B, respectively, followed by a sample index number.

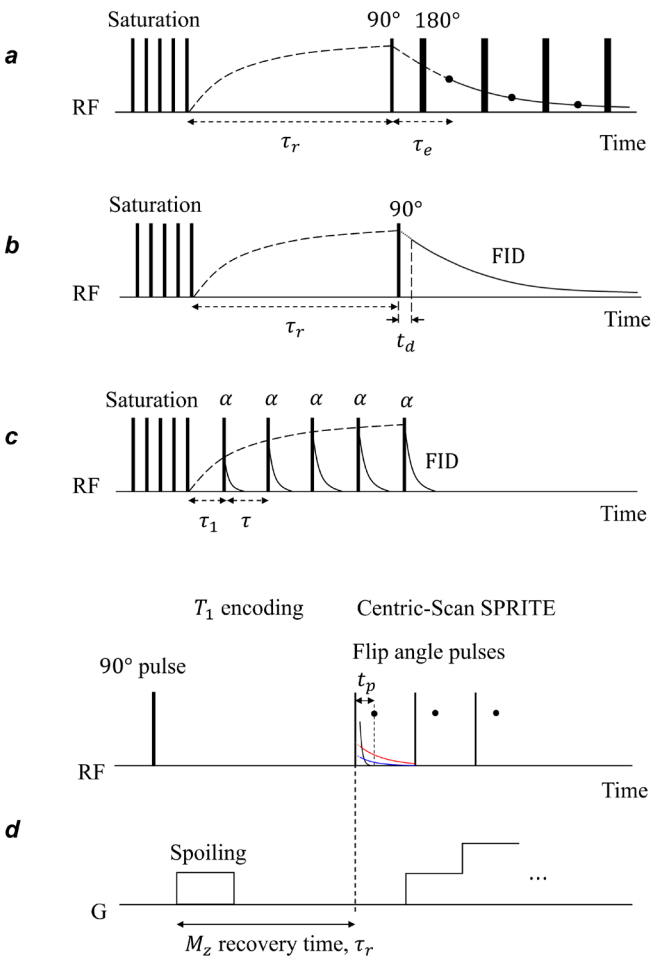

Fig. 1. Schematic diagrams of pulse sequences for (a) T_1-T_2 measurement, (b) T_1-T_2^* measurement, (c) Look-Locker T_1^*-T_2^* measurement, and (d) centric-scan SPRITE with magnetization preparation. The FID decays for oil (red), water (blue), and kerogen (black) are shown separately for illustration purposes. The kerogen FID fully decays before signal detection in the Centric scan SPRITE measurement. T_1-T_2^* measurement provides a better resolution in time compared to T_1-T_2 measurement. Look-Locker T_1^*-T_2^* measurement acquires multiple FIDs during a single T_1 recovery and is therefore drastically faster than T_1-T_2^* measurement.

Water adsorption and desorption experiments were performed at a controlled relative humidity of 0.75 and near 0, respectively, in a desiccator at a temperature of 24 ℃. This allowed manipulation of the water content in shale samples, leaving oil and kerogen content intact. Evaporation experiments were conducted by placing the samples in an oven that was set to 60 ℃. This caused the oil and water content of the samples to decrease, leaving kerogen content intact. Step pyrolysis experiments were performed by exposing the samples to elevated temperatures up to 850 ℃ in the presence of helium. This caused kerogen content to decrease and thermally dissociate to generate hydrocarbon. The water uptake experiments were performed by bringing the bottom face of the sample in contact with 3 wt% KCl brine. This initiated water imbibition into the samples.

Table 1. Summary of experiments conducted on various shale samples.

Sample ID	Formation	Field (T)	Experiment
EG4	Eagle Ford	2.4	Comparison of T_1-T_2^* and T_1-T_2 measurement
EG13	Eagle Ford	0.2	
EG4	Eagle Ford	2.4	Water adsorption/desorption and evaporation coupled with T_1-T_2^* measurement
EG12	Eagle Ford	4.7	Step pyrolysis coupled with T_1-T_2^* measurement
EG12	Eagle Ford	4.7	Comparison of T_1-T_2^* and Look-Locker T_1^*-T_2^* measurement
EG13	Eagle Ford	0.2	
EG10 EG11	Eagle Ford	2.4	1D and 3D imaging of natural fluid content
M5	Marcellus		
B5	Barnett		
EG10 EG11	Eagle Ford	2.4	Water uptake

3.3 Instrumentation

The MR measurements were conducted using three instruments. (1) A Nalorac (Martinez, CA) horizontal bore superconducting magnet with magnetic field strength of 2.4 T, equipped with a custom-built birdcage RF probe, 4.5 cm id, driven by a 2 kW Tomco (Tomco Technologies, Stepney, Australia) RF amplifier. The RF probe had a 90° pulse duration of 10.5 µs and probe deadtime of 24 µs. The water-cooled Nalorac gradient set driven by Techron (Elkhart, IN) 8710 amplifiers provided maximum gradient strengths of 25 G/cm in the three principal directions. The console was a Tecmag (Houston, TX) Redstone. (2) A vertical bore 4.7 T superconducting magnet (Cryomagnetics, Oak Ridge, TN) was driven by a Redstone console (Tecmag, Houston, TX). The RF probe was a Doty DS1-874 (Doty Scientific, Columbia, SC) birdcage with 2.1 cm id driven by a 2 kW Tomco RF amplifier (Tomco Technologies, Stepney, Australia), with a 90° pulse duration of 23 µs and probe deadtime of 20 µs. (3) A MARAN DRX-HF (Oxford Instruments Ltd, Abingdon, Oxford, UK) vertical bore permanent magnet provided a magnetic field of 0.2 T. The RF probe was a custom-built solenoid 12 cm in length with a 4.5 cm id with a 90° pulse duration of 15 µs and probe deadtime of 43 µs. MR measurements performed using instruments (1) and (2) are referred to as high field measurements throughout the text, whereas those conducted using instrument (3) are considered low field measurements.

4 Results and discussions

4.1 Resolving shale signal species using T_1-T_2 and T_1-T_2^* measurements

T_2^* can be measured with a much better time resolution compared to T_2. Figure 2 compares FID and CPMG measurements for shale sample EG13. The FID measurement offered a significant improvement in time resolution compared to the CPMG measurement. CPMG measurement is limited by the echo time, τ_e, which is commonly in the order of hundreds of microseconds. The transverse magnetization in Figure 2 was measured with an echo time of 200 µs and is sampled at intervals of the echo time. In the FID, however, data acquisition started after a deadtime, t_d of 43 µs with sampling at a dwell time, dw of 1 microsecond. Data sampling frequency in FID is improved by at least two orders of magnitude compared to CPMG, which results better time resolution of the decay. Figure 2 demonstrates that (1) the CPMG approaches FID decay curve for samples with fast-decaying signal components, as indicated in Eq. 1, (2) FID gives a higher resolution in time compared to CPMG. The fast-relaxing kerogen signal is completely missed in the CPMG measurement while it was acquired in the FID.

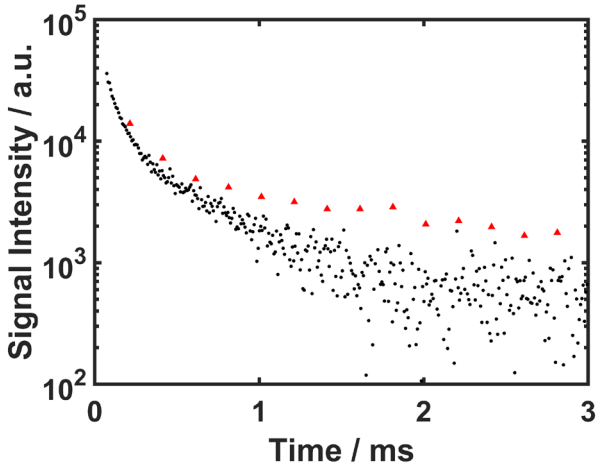

Fig 2. Comparison of FID (circles) and CPMG (triangles) measurements at low field for shale sample EG13. The FID approaches the CPMG at early times. Better time resolution is achieved using the FID compared to the CPMG. Kerogen signal is missed by the CPMG because of the echo time limitation.

Figure 3 shows 2D T_1-T_2 and T_1-T_2^* relaxation correlation measurements of two shale samples at high and low field. Signal components in Figure 3 are marked with their corresponding shale species, integrated signal intensity, and log-mean relaxation times.

Water in shale undergoes a strong surface relaxation. Its signal peak yielded a short T_1 of ~1 ms and low T_1/T_2 and T_1/T_2^* ratios. The coordinates of the water signal peaks in the T_1-T_2 and T_1-T_2^* relaxation correlation maps did not depend on the field strength. Oil in the shale samples had large T_1/T_2 and T_1/T_2^* ratios which yielded a long T_1 of ~ 159 ms at high field and a T_1 of ~38 ms at low field measured using T_1-T_2^* measurement, as shown in Figures 3b and 3d. The oil T_1 was significantly affected by the field strength. Such effects of field strength on the T_1 of water and oil in shales has been reported elsewhere [15,21]. Kerogen relaxation is dominated by dipolar interactions which causes very short transverse relaxation times and large diagonal value peak (T_1/T_2 and T_1/T_2^* ratios). Kerogen yielded a T_2^* of ~ 10 us, and a long T_1 of ~ 250 ms at high field and T_1 of ~30 ms at low field. Kerogen also showed a significant T_1 variation with the field strength. Figures 3b and 3d provide evidence of T_1

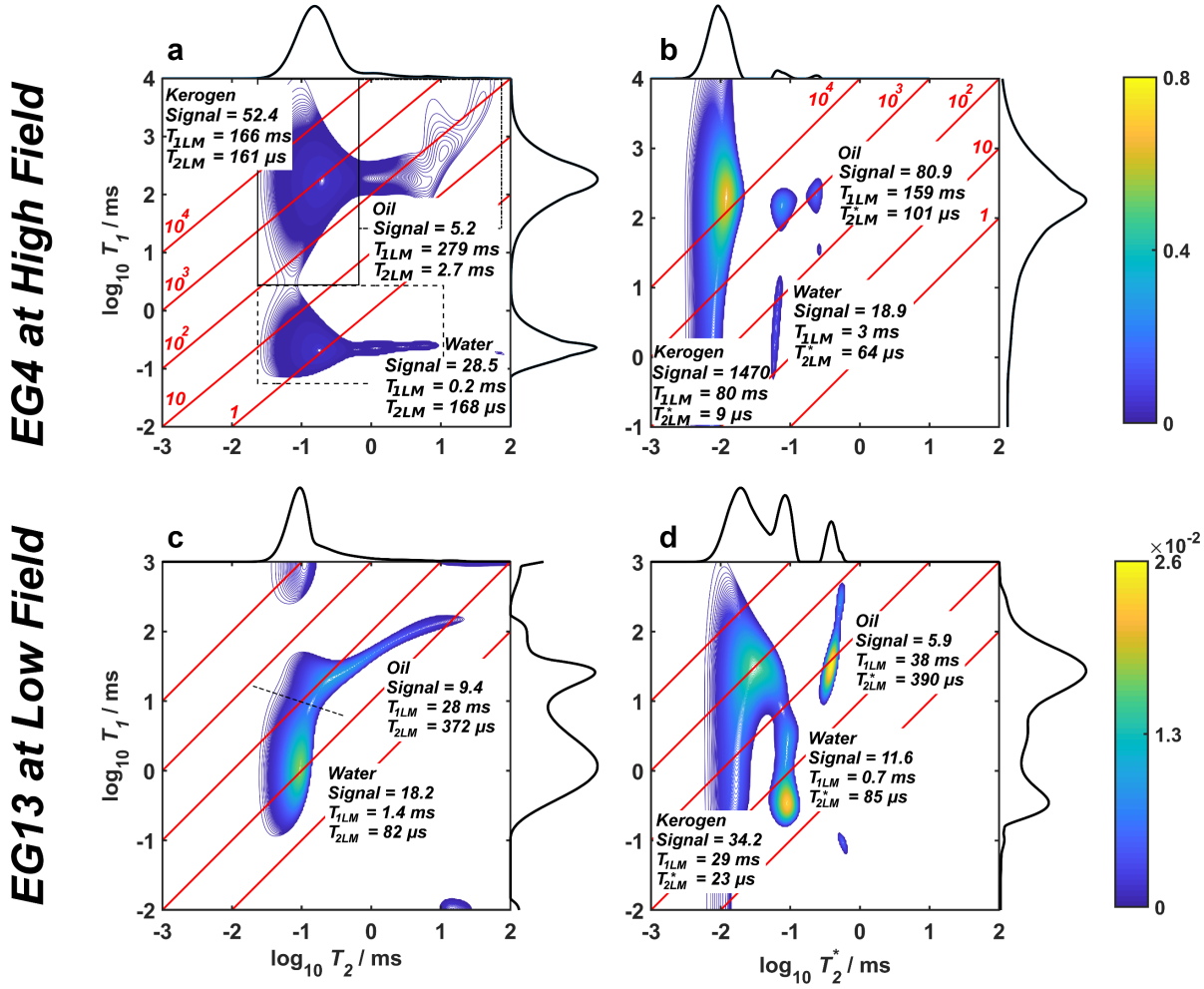

Fig. 3. Comparison of T_1-T_2 measurement (a and c) and T_1-T_2^* measurement (b and d) performed at 2.4 T and 0.2 T. Shale signal species, oil, water, and kerogen are better resolved and quantified using T_1-T_2^* measurement. Integrated signal intensity and T_2 log-mean for each signal peak is shown next to the peak. The diagonal lines show relaxation time ratios (T_1/T_2^* or T_1/T_2) of 1, 10, 10^2, 10^3, and 10^4. The values of the diagonals are the same in all subfigures.

dependency on the field strength for kerogen, similar to that for oil. This is consistent with the BPP relaxation model of dipolar interaction for solid like materials.

Shale signal components overlap in the T_1-T_2 relaxation correlation plot. The overlap of shale signal deters fluid quantification. As shown in Figure 3a, at high field, the kerogen signal peak overlaps with that of oil and water. Furthermore, the T_1 dependency of oil in shales on the field strength caused oil and water signal peaks to overlap at low field in the T_1-T_2 relaxation correlation plot of Figure 3c. T_1-T_2^* relaxation correlation measurement, by contrast, provides the adequate resolution to discriminate kerogen, oil, and water signal peaks at both high and low fields as shown in Figures 3b and 3d.

A significantly better time resolution of transverse relaxation lifetime is achieved using the T_1-T_2^* method compared to the T_1-T_2 method. In T_1-T_2^* measurement, signal detection begins a few microseconds after the RF pulse, unlike T_1-T_2 measurement in which that starts after an echo time of hundreds of microseconds. Furthermore, the rate of data collection in the T_1-T_2^* measurement is improved by at least two orders of magnitude. This improved time resolution allows better discrimination of signal components.

As shown in Figure 3c, the kerogen signal was not visible in the T_1-T_2 relaxation correlation plot at low field due to the echo time limitation. At high field, in Figure 3a, the kerogen signal peak was shifted to a higher T_2 value and its detected integrated signal intensity was reduced significantly in T_1-T_2 relaxation correlation map. This leads to overlap of signal peaks in the T_1-T_2 relaxation correlation map, which hampers signal differentiation and quantification. Therefore, Shale signal components are better resolved and quantified using the T_1-T_2^* relaxation correlation measurement. Moreover, comparing Figure 3b and 3d, the kerogen signal contribution to the total shale signal is reduced for the measurement at low field. This is due to the long deadtime of 43 µs for the low field instrument compared to the decay lifetime of kerogen. It is worth mentioning that this is not a characteristic of all low field measurements. In principle, a low field measurement with a short deadtime should be capable of giving correct signal contributions for all shale signal species.

4.2 Fluid quantification using T_1-T_2^* measurement

In this section, water and oil content of a shale sample is manipulated systematically to calibrate the MR signal with the fluid content. This helps not only to unambiguously

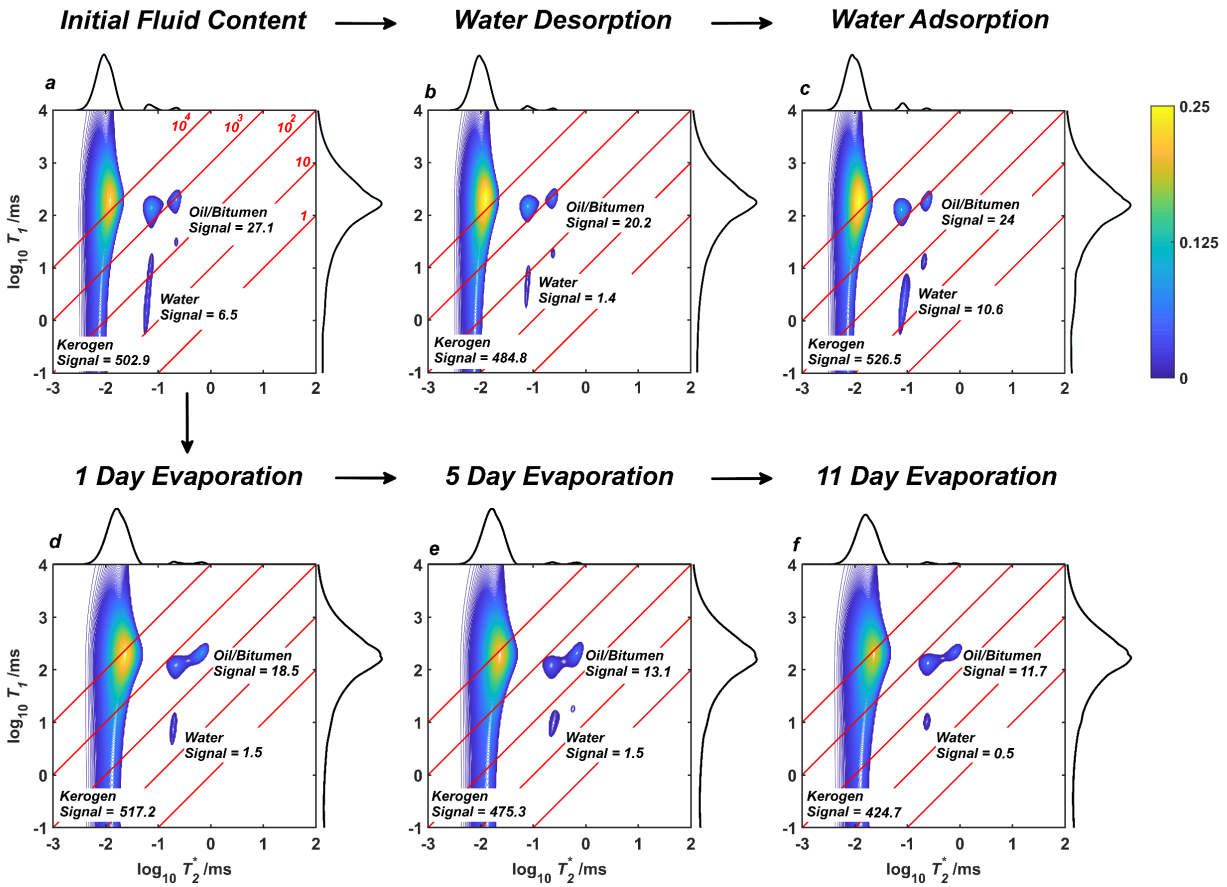

Fig. 4. T_1-T_2^* measurement for sample EG4 undergoing water adsorption/desorption and evaporation experiments. T_1-T_2^* measurement (a) at the as-received condition, (b) after water adsorption (c) after water desorption (d) after 1 day of evaporation (e) after 5 days of evaporation (f) after 11 days of evaporation. Water peak signal intensity varied when shale water content was manipulated during water adsorption/desorption experiments. Kerogen and oil signal intensities remained constant. Water and oil signal intensities decreased during evaporation experiments. Kerogen intensity remained constant.

distinguish water, oil, and kerogen signal components in the relaxation correlation plot but also to quantify shale fluid content. Figure 4a shows the T_1-T_2^* measurement of a shale sample in its as-received condition. This shale sample was subjected to two sets of experiments (1) water adsorption/desorption and (2) evaporation experiments.

The water adsorption/desorption experiments were performed using 40.84 gr crushed shale sample in desiccator with controlled relative humidity at room temperature to manipulate water content of the shale sample. Figure 4b and 4c show the T_1-T_2^* relaxation correlation measurement of the shale sample after water desorption and after water adsorption, respectively. Water integrated signal intensity decreased from 6.5 to 1.4 after water desorption and increased to 10.6 after water adsorption. Oil signal intensity decreased slightly, while kerogen signal intensity remained relatively constant. Some light oil components may have evaporated in the desiccator and left the sample, resulting in the 20% reduction in the oil signal.

During the evaporation experiments, water and oil content in 10.46 gr of crushed shale sample decreased. Figures 4d-f show the T_1-T_2^* measurement after 1, 5, and 11 days. The integrated signal intensity of the signal peaks associated with water and oil reduced while kerogen integrated signal intensity remained relatively unchanged. The slight decrease in the kerogen signal intensity is likely due to loss of a minor amount of the powered sample between measurements.

The integrated signal intensity of the resolved MR signal of shale species in the T_1-T_2^* relaxation correlation plot gives linear relationships with their corresponding shale species. This is a foundation for fluid quantification in shales. In Figure 5a, the water integrated signal intensity is calibrated for water content in the shale sample by a plot of the sample's mass change due to change in the sample's water content with the resolved integrated signal intensity of water in the T_1-T_2^* measurement. The initial water content of the sample is calculated to be 0.24 gr water / 100 gr rock. Having the water calibration curve, the mass loss due to water vaporization, in the evaporation experiment, can be calculated to give sample's mass loss due to oil evaporation. This allows calibration of oil signal in Figure 5b. The initial oil content of the sample is calculated to be 0.98 gr oil / 100 gr rock.

4.3 Kerogen characterization

A step pyrolysis experiment coupled with T_1-T_2^* relaxation correlation measurements were performed to manipulate kerogen signal in the shale samples. The integrated signal intensity of kerogen, oil, and water resolved using the T_1-T_2^* relaxation correlation measurement was determined after

each pyrolysis step. The integrated signal intensities were then converted to hydrogen content of shale species in moles using a reference sample which had a known hydrogen content.

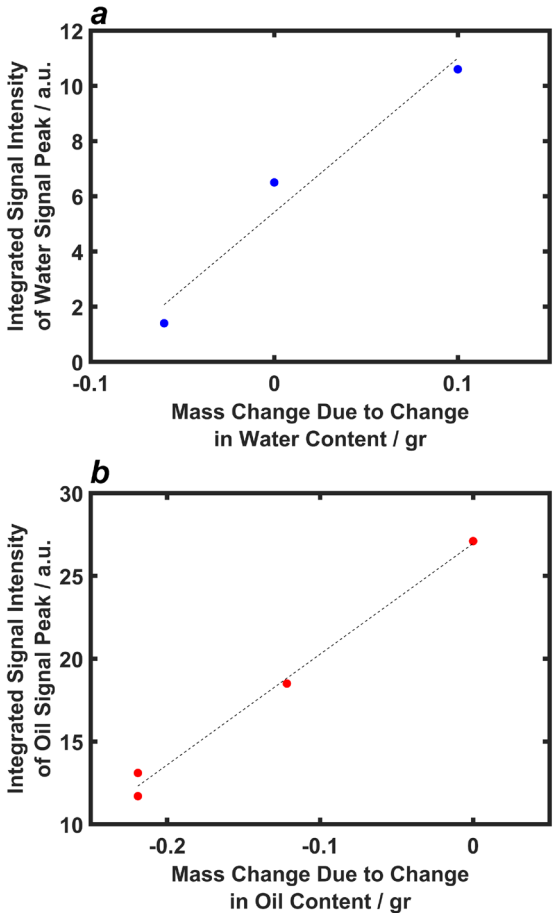

Fig. 5. (a) Water and (b) oil integrated signal intensity obtained from T_1-T_2^* measurement versus sample mass change due to change in the respective fluid content shows a linear relationship that is used to calibrated signal and give shale water and oil content.

Figures 6a show the hydrogen contents of kerogen, oil, and water relative to its initial values. Figure 6b shows a thermogravimetric analysis (TGA) and its derivative (DTG) for the shale sample. The water vaporization from the sample is evident in the DTG analysis at 100 ℃. The water evaporation in TGA is consistent with the hydrogen water content determined using the T_1-T_2^* measurement. The short relaxation signal component in the T_1-T_2^* measurement decreased at a temperature range that is similar to that of kerogen pyrolysis. Furthermore, hydroxyls in clay minerals are commonly pyrolyzed at 600-1000 ℃ [34]. Therefore, the short relaxation signal component is dominated by the hydrogen content of the shale sample in the form of kerogen.

The hydrogen content in kerogen was calculated to be 1.05 mol/100 gr rock. The kerogen hydrogen content in shales is the most important chemical benchmark to determine its hydrocarbon potential. A kerogen class I to IV has decreasing amount of hydrogen in its structure. Additionally, comparing shale samples from the same formation, an immature kerogen has greater hydrogen quantity [35].

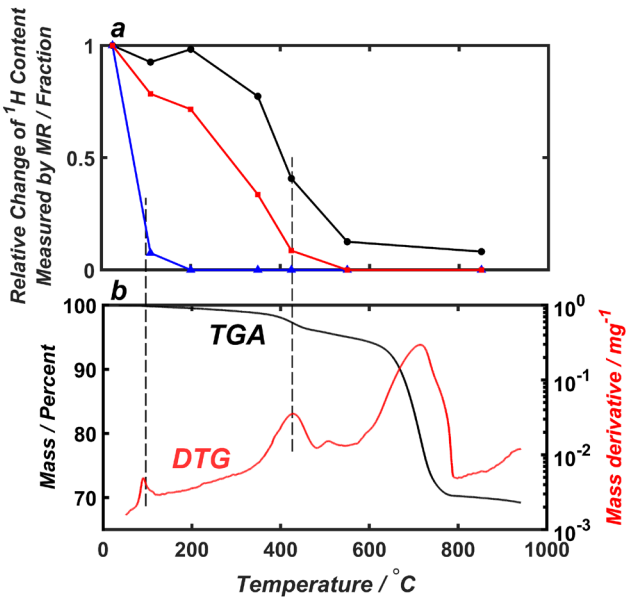

Fig. 6. (a) Change of hydrogen content relative to its initial value as a function of pyrolysis temperature. The hydrogen contents of kerogen (black), oil (red), and water (blue) in the shale sample are determined using calibration of signal from T_1-T_2^* measurement. (b) thermogravimetric analysis (TGA) of shale sample measuring mass loss versus pyrolysis temperature. DTG shows the derivative of the TGA curve that distinguishes peaks. Water peak in DTG at temperature ~100 ℃ is consistent with the water content measured using MR. The decrease in kerogen hydrogen content from the short transverse relaxation lifetime of T_1-T_2^* measurement is consistent with the DTG kerogen peak at 425 ℃.

4.4 Look-Locker T_1^*-T_2^* relaxation correlation at low field

Figure 7 compares Look-Locker T_1^*-T_2^* and T_1-T_2^* relaxation correlation measurements for two nominally similar shale samples. 10.8 gr of sample EG12 and 134.62 gr of sample EG13 were measured at low and high field, respectively. The instrument sensitive volume for the high field measurements was smaller than that for the low field measurements. Therefore, a smaller quantity of shale sample was used for the high field measurements. This should be considered when comparing low and high field measurements presented here. Since signal strength is proportional to the amount of hydrogen present for the measurement. In the Look-Locker T_1^*-T_2^* plots, the integrated signal intensities in arbitrary units are corrected based on Eq. 2b and are shown next to each signal peak.

Shale species are adequately resolved in both Look-Locker T_1^*-T_2^* and T_1-T_2^* relaxation correlation plots. Integrated signal intensities for oil and water signal peaks measured by T_1-T_2^* measurement are close to those obtained by Look-Locker T_1^*-T_2^* measurement for both samples. The signal intensities shown in Figure 7a-d are calibrated using a reference sample with known hydrogen content to give the oil and water content in gr per 100 gr of rock. It is assumed that water and oil have the same hydrogen density. Figure 7e shows that the fluid content obtained using Look-Locker T_1^*-T_2^* and T_1-T_2^* measurements are similar. This allows quantifying fluid content in shales using Look-Locker T_1^*-T_2^* measurement. Kerogen signal intensity is underestimated at

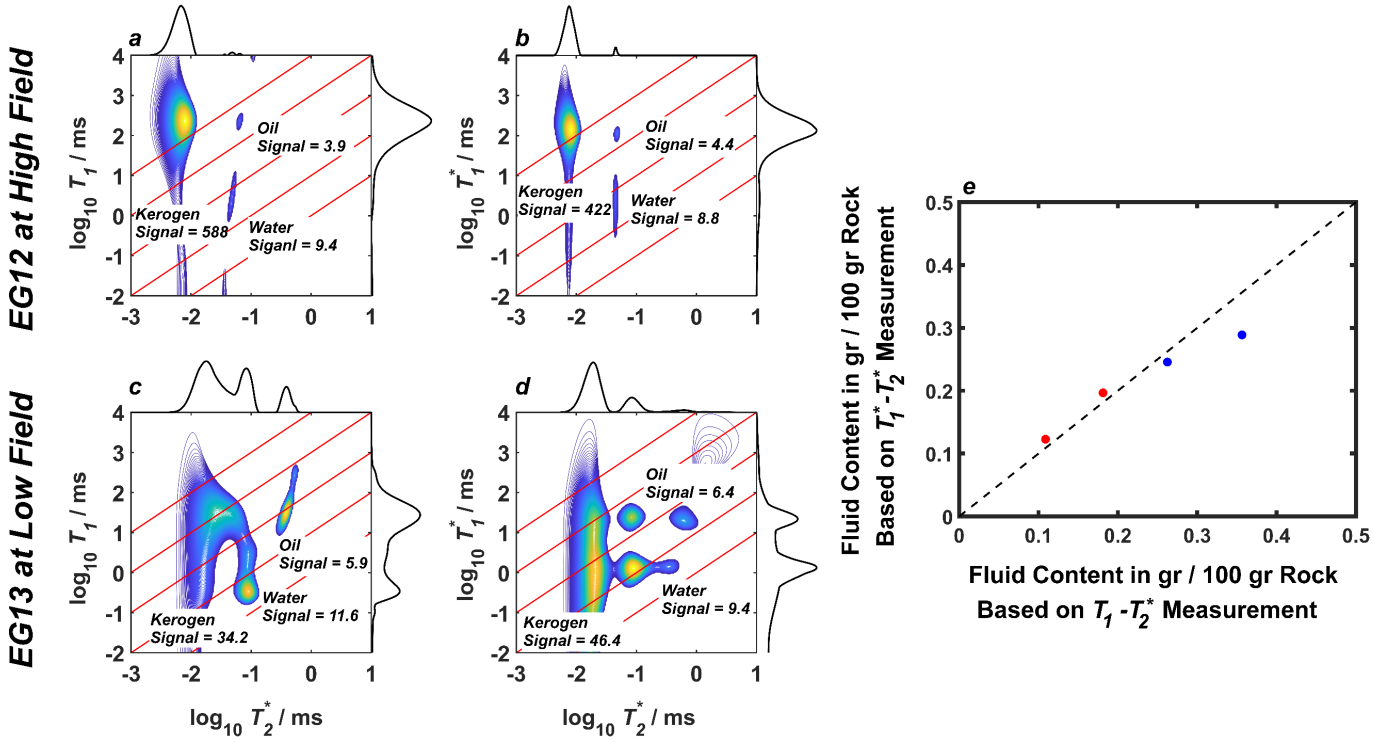

Fig. 7. Comparison of T_1-T_2^* measurement (a and c) and Look-Locker T_1^*-T_2^* measurement (b and d) performed at 4.7 T and 0.2 T for samples EG12 and EG13, respectively. Shale signal species, oil, water, and kerogen are resolved and quantified using both measurement methods. T_1^*-T_2^* measurement is much faster compared to T_1-T_2^* measurement. The integrated signal intensities next to each signal peak for the T_1^*-T_2^* measurement are corrected using Eq. 2b. (e) Fluid quantities determined using T_1-T_2^* measurement versus that measured using T_1^*-T_2^* measurement. Similar values for fluid quantities are determined. The blue and red data points represent water and oil content, respectively. The dashed line is the simple diagonal.

low field since it was measured using a long deadtime compared to the kerogen decay lifetime.

In comparison with the T_1-T_2^* method, the Look-Locker T_1^*-T_2^* method provides sufficient resolution to resolve and quantify shale fluids while reducing measurement time significantly. Application of Look-Locker T_1^*-T_2^* method becomes especially beneficial at low field due reduced sensitivity. Measurement time for the T_1-T_2^* method was 30 min giving a SNR of 453, and 2.5 hr with a SNR of 81 at high and low field, respectively. Look-Locker T_1^*-T_2^* measurement took 1 min at high field yielding a SNR of 93 and 17 min at low field giving a SNR of 40.

In Figure 1c, FIDs are acquired at linearly spaced T_1 recovery times. Therefore, this measurement is suitable for samples that yield sufficiently close T_1 relaxation times. Shale signals meet this requirement. The Look-Locker T_1^*-T_2^* method is able to resolve and quantify shale signal components.

The Look-Locker T_1^*-T_2^* method using more common low field MR scanners will give fast, non-invasive, and accurate shale fluid content for shale drill cuttings at the wellsite and core plugs in the laboratory.

4.5 Imaging shale samples

Shale signal components resolved in the T_1-T_2^* measurement can be employed to understand and guide the invoked contrast in the SPRITE imaging method. The kerogen signal can be excluded from the image signal by choosing a sufficiently long t_p to allow kerogen signal to fully decay but short enough to acquire the shale fluid signals. The remaining signal can be resolved for oil and water based on their T_1 contrast detected by the T_1-T_2^* measurement. Application of this imaging technique gives separate oil and water images in core plug size samples.

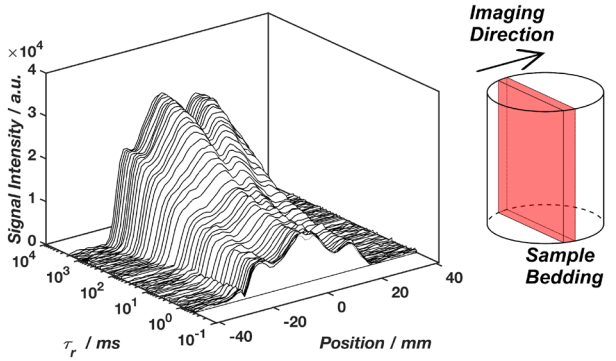

Fig. 8. T_1-weighted 1D images of sample EG11 perpendicular to the sample beddings. The images show T_1 recovery of magnetization during τ_r with position. Reproduced with permission from Chemical Engineering Journal (2022) 428, 131042 [25].

Figure 8 shows a series of T_1-weighted images of shale sample EG11 acquired using 1D centric-scan SPRITE method described in Section 3.1.2. The images were acquired perpendicular to the bedding structure of the samples to reveal contrast in their oil and water content. Figure 8 shows T_1 recovery of magnetization as T_1 encoding time, τ_r increases.

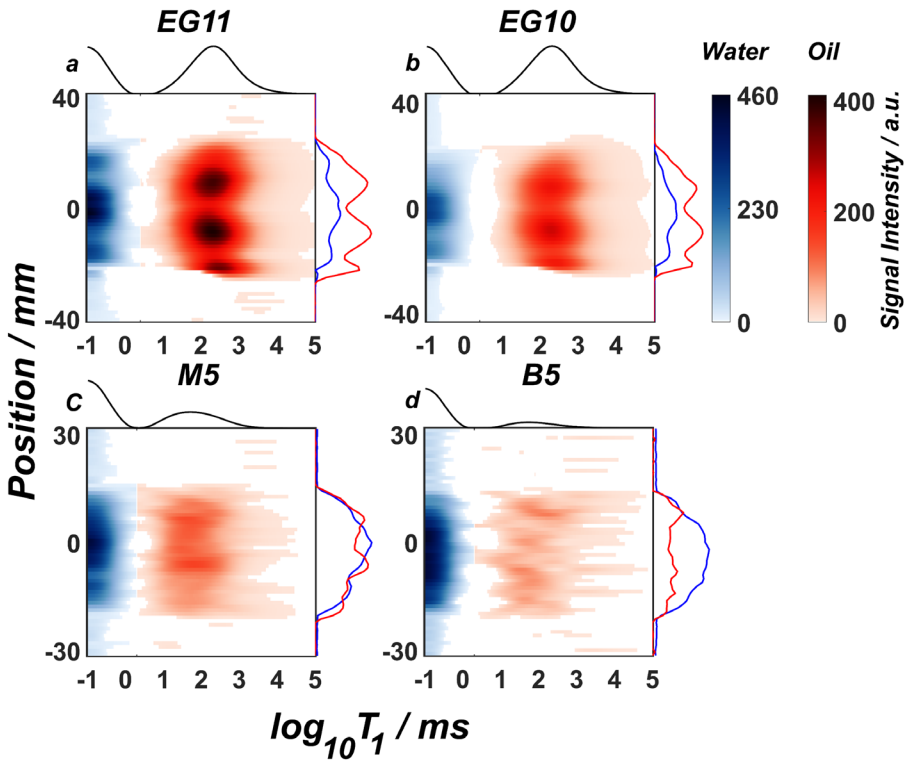

Fig. 9. T_1 resolved 1D images for (a) EG11 from Eagle Ford Formation, (b) EG10 from Eagle Ford Formation (c) M5 from Marcellus Formation, and (d) B5 from Barnett Formation. The projections on the horizontal axes is the bulk T_1 distribution of the sample after kerogen signal was excluded. The blue projection on the vertical axes is the projection of short T_1 component indicating water image, and the red one is the projection of long T_1 component representing oil image. The oil and water profiles spike alternatively. Reproduced with permission from Chemical Engineering Journal (2022) 428, 131042 [25].

4.5.1 Natural fluid storage in shales – wettability

The data shown in Figure 8 was processed using Eq. 4 to resolve the image signal for oil and water in the T_1 relaxation time. Three more shale samples, EG10, M5, and B5 from different formations in their as-received condition, were processed using the same method. Figure 9 shows the spatially resolved T_1 after exclusion of kerogen signal. The long T_1 signal component is attributed to the oil in the shale samples, and the short T_1 signal species is associated with the shale water content. The projection of the signal on the horizontal axis gives the bulk T_1 relaxation time of the sample after exclusion of kerogen signal. The integrated signal intensity of the long T_1 signal peak shown on the vertical axis in red gives the oil image in the sample, and the integrated signal intensity of the short T_1 signal component on the same axis in blue yields the water image.

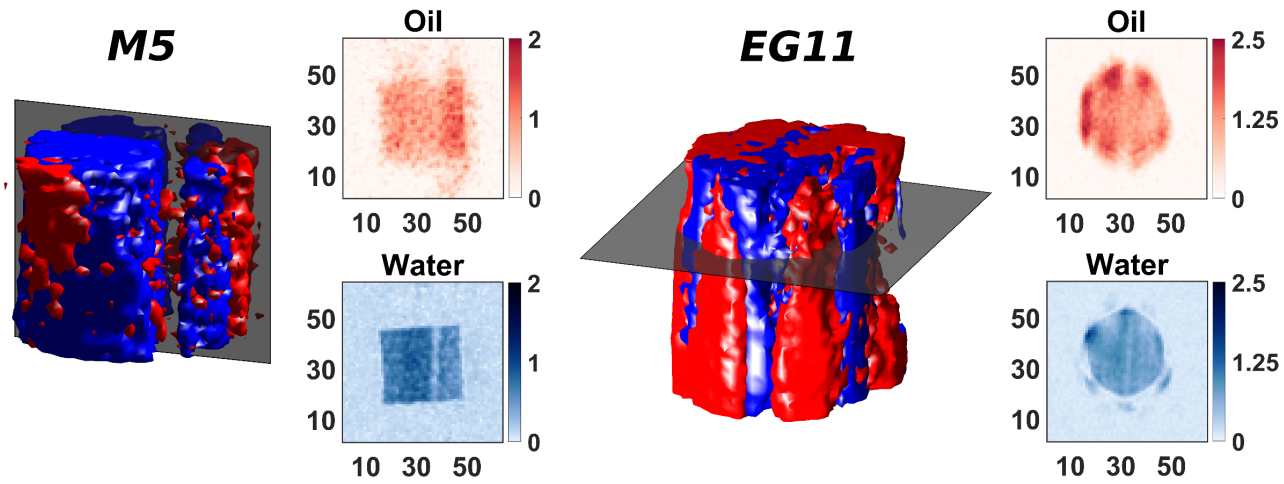

Fig. 10. Superimposed 3D images of water and oil in shale samples M5 and EG11. The cross sections show signal intensity converted to fluid content in porosity unit (p.u.). Fluid distribution is controlled by the bedding structure of the samples. The signal void in sample M5 is indication of a low porosity layer. Axis for cross sections show pixel numbers. Image FOV was 80 mm. Reproduced with permission from Chemical Engineering Journal (2022) 428, 131042 [25].

The high degree of shale heterogeneity demands 3D imaging. The imaging scheme in Figure 1 was also employed using 3D centric-scan SPRITE to give 3D images of oil and water. The superimposed 3D images of oil and water for samples EG11 and M5 in their as-received condition are shown in Figure 10. The 3D images were calibrated using a reference sample to give quantity of fluids. The oil hydrogen index was assumed to be similar to that of water. The cross sections of the 3D images in Figure 10 show the water and oil content in porosity unit (p.u.).

The core plug scale heterogeneity of shale samples is commonly characterized by their bedding structure. The 1D images of oil (red) and water (water) in various shale samples in Figure 9 show alternating oil-rich and water-rich layers. The oil images show a crest at the trough of the water images. This means the pore space in some layers is mostly occupied by water, while the pore space in other layers is largely prone to oil.

The degree and nature of the shale heterogeneity can be characterized by how it manifests as variation in the fluid saturation. A 1D image of a sample with homogenous fluid saturation acquired with an image direction shown in the schematic core plug in Figure 8 yields a semicircle. Figure 9d shows such characteristics in the 1D image of sample B5. Alternating oil-rich and water-rich layers indicates spatial wettability variation. A layer with a higher clay content is more likely to be water-rich since it is naturally water-wet, while a layer with more organic kerogen content may be more favourable to the oil phase. The superimposed 3D image of oil and water in the sample EG11 also shows the sample's layered structure. The image intensity of the cross sections in Figure 10 is calibrated to give oil and water content in porosity unit. For sample M5, in Figure 10, the signal void in the oil and water images is due to a low porosity layer, since no fracture is visible on the periphery of the core plug.

4.6 Water uptake

The key role of shale core plug scale heterogeneity on the fluid storage, discussed in Section 4.5, motivates study of its impact on the fluid flow in shales. This was investigated by performing water uptake experiments on two nominally similar samples, EG10 and EG11. The water uptake experiments were monitored using gravimetric measurements, T_1-T_2^* method, and 3D centric-scan SPRITE imaging method with T_1 suppression for 30 days.

4.6.1 T_1-T_2^* measurements

Figure 11 shows T_1-T_2^* measurements of samples EG10 and EG11 before and after water uptake experiment. Water integrated signal intensity increased for both samples during water uptake experiment.

The high resolution of T_1-T_2^* method allowed measuring the sample EG11 with a reference sample. The reference sample composition was 17.0 wt% H_2O, 82.9 wt% D_2O and 0.07 wt% $CuSO_4$ and contained 3.1 mmol of ^1H. The signal peak from the reference sample of known hydrogen content is shown in green in the T_1-T_2^* measurements of Figure 11. The position of the signal peak from the reference sample in the T_1-T_2^* relaxation correlation plot was adjusted by varying the concentration of $CuSO_4$. This signal peak was well-resolved from the shale signal species. Therefore, it did not interfere with quantification of shale signal components. The employment of a reference sample (1) aids in production of consistent results between measurements because the signal

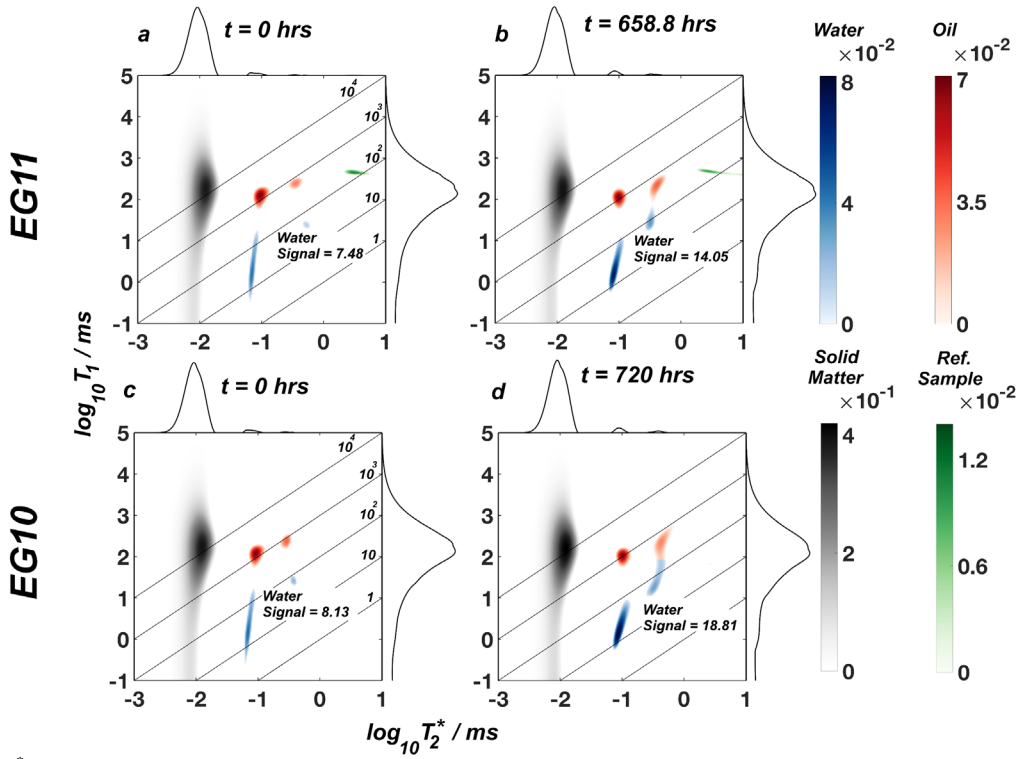

Fig. 11. 2D T_1-T_2^* relaxation correlations of sample EG11 and EG10 (a and c) before and (b and d) after water uptake, respectively. Kerogen, water, oil, and reference sample signals are resolved and are shown in gray, blue, red, and green, respectively. The water peaks show an increase in signal intensity with water uptake. Reproduced with permission from Chemical Engineering Journal (2022) 428, 131042 [25].

properties of the reference sample remain constant between measurements. This becomes particularly significant when T_1-T_2^* measurements of multiple samples are to be compared or when T_1-T_2^* responses of a sample are measured during a process. (2) A reference sample can be used to convert MR signal for shale signal species to their hydrogen content. It should be noticed that the poor signal differentiation by the T_1-T_2 method prevents application of such reference sample. Signal discrimination is hampered in the T_1-T_2 method compared to T_1-T_2^* method for shales. Therefore, the overlap of signal components will further impair quantification of shale signal intensities using T_1-T_2 methods. As shown in Figure 11, the T_1-T_2^* method was capable of resolving and quantifying multicomponent signals, even when four signal components are present.

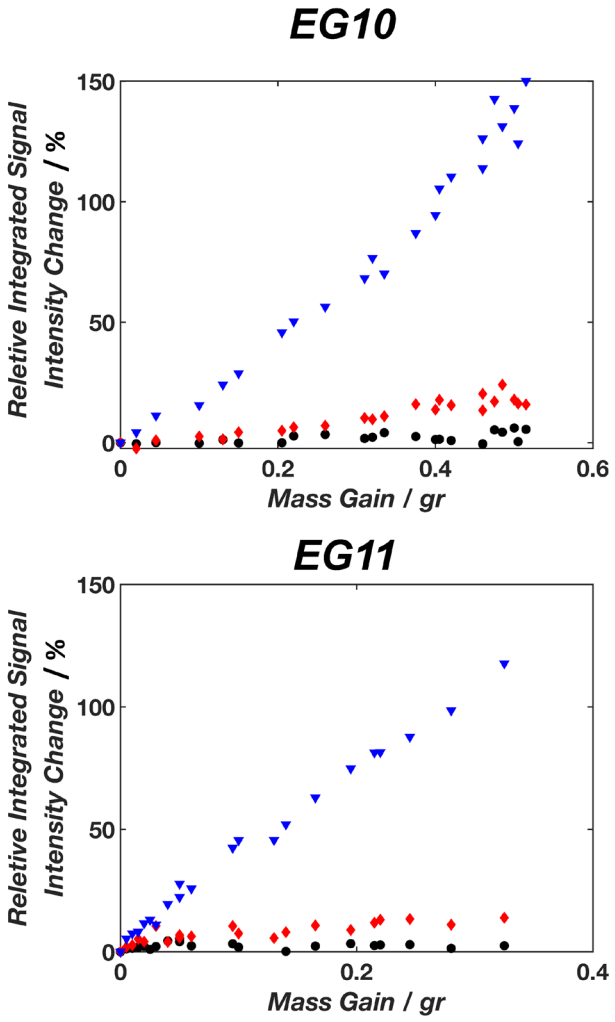

Fig. 12. Relative signal change of water peak (▼), oil (◆), and kerogen (●) signal peaks versus mass gained by (a) sample EG10 and (b) sample EG11, based on the T_1-T_2^* measurements during water uptake experiments. Kerogen and oil signal intensities remained essentially unchanged. Water signal intensity in the T_1-T_2^* relaxation correlations showed a linear relationship with shale water content.

Relative integrated signal intensity change ($\frac{S(t)-S(t=0)}{S(t=0)} \times 100$) in Figure 12 for oil and kerogen shale signal components remained constant, while that of water changed during water uptake experiments for both shale samples. Water signal component showed a linear relationship with the sample mass gain due to water uptake. This not only confirms the identification of water signal peak, but also allows accurate quantification of water content in the shale samples.

4.6.2 Imaging during water uptake

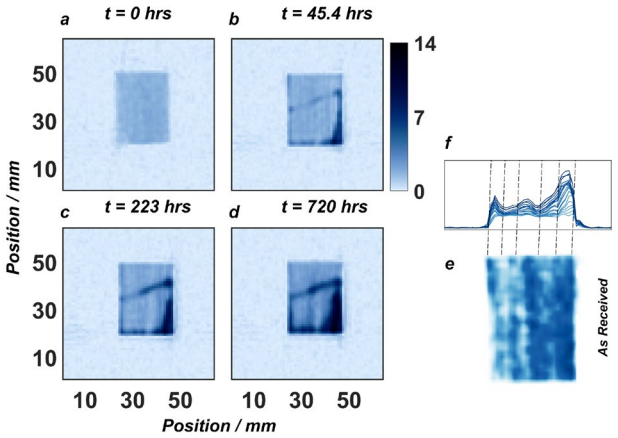

Fig. 13. 2D cross sections (a to d) extracted from oil suppressed 3D centric-scan SPRITE measurements perpendicular to the beddings of EG10 sample with time during water uptake experiment. The signal intensity is calibrated to the water content in porosity units. 2D cross section (e) from oil suppressed 3D centric-scan SPRITE image shows sample EG10 in its as received condition. 1D water profiles (f) are projections of the water content in the 2D cross sections as water uptake proceeds. The dashed lines demonstrate that beddings identified in the as received condition control the water transport during water imbibition. Water uptake in the EG10 sample reveals the layered structure of the sample and the fracture across the sample. Reproduced with permission from Chemical Engineering Journal (2022) 428, 131042 [25].

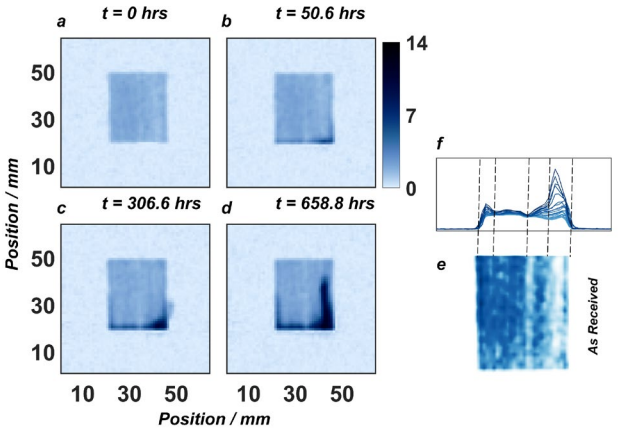

Fig. 14. 2D cross sections (a to d) extracted from oil suppressed 3D centric-scan SPRITE measurements perpendicular to the beddings of EG11 sample with time during water uptake experiment. The signal intensity is calibrated to the water content in porosity units. 2D cross section (e) from oil suppressed 3D centric-scan SPRITE image shows sample EG11 in its as received condition. 1D water profiles (f) are projections of the water content in the 2D cross sections as water uptake proceeds. The dashed lines demonstrate that beddings identified in the as received condition control the water transport during water imbibition. Water uptake in the EG11 shale sample reveals the layered structure of the sample. Reproduced with permission from Chemical Engineering Journal (2022) 428, 131042 [25].

Figure 13 and Figure 14 show 2D slices from 3D images acquired using centric-scan SPRITE imaging method with T_1 suppression for samples EG10 and EG11, respectively, undergoing water uptake. The image intensity was converted to water content in porosity unit using a reference sample. The water imbibition, in Figures 13 and 14, followed the bedding structure of the sample. This shows that wettability variation between the sample beddings, also detected for shale samples in their as-received condition, plays an important role in the fluid flow. Figure 13 shows a visible fracture that was filled with water as water uptake continued.

5 Conclusion

This work presents magnetic resonance methods and their application for quantitative signal detection for shale characterization. It was shown that T_1-T_2^* relaxation correlation measurement differentiated and quantified the short-lived multicomponent MR signal in shales. The Look-Locker T_1^*-T_2^* measurement was demonstrated to give quantitative shale signal with high sensitivity even at low field. The SPRITE imaging method with magnetization preparation was used to give 1D and 3D images with a field of view of 8 cm. Millimetre scale heterogeneities in shale samples were identified using the imaging technique. These heterogeneities were imposed on water and oil content by the samples' laminae. Water absorption/desorption and evaporation experiments were used to calibrate MR signal to give oil and water content. Step pyrolysis experiments showed that the short transverse signal lifetime is dominated by the kerogen content. Water uptake experiments coupled with MR imaging and T_1-T_2^* measurement demonstrated the key role of wettability in determining transport in shales.

Application of these methods for shale core analysis in the laboratory and for shale drill cuttings enhances estimation of reservoir quality and ensures economic hydrocarbons production from shale reservoirs.

S. Zamiri thanks the New Brunswick Innovation Foundation for a scholarship and University of New Brunswick for the Gerald I. Goobie Chemical Engineering Scholarship. Bruce J. Balcom acknowledges NSERC of Canada for a Discovery grant [2015-6122] and the Canada Chairs program for a Research Chair in Material Science MRI [950-230894].

References

1. R. Rezaee, *Fundamentals of Gas Shale Reservoirs* (John Wiley & Sons, Inc, Hoboken, 2015)
2. Y. Zee Ma, S.A. Holditch, *Unconventional Oil and Gas Resources Handbook* (Elsevier, 2016)
3. Y. Wang, S. Xu, F. Hao, B. Zhang, Z. Shu, Q. Gou, et al., Geol Soc Am Bull 132, 1704–21 (2020)
4. R.G. Loucks, R.M Reed, S.C. Ruppel, U. Hammes, AAPG Bull 96, 1071–98 (2012)
5. L. Zhang, B. Li, S. Jiang, D. Xiao, S. Lu, Y. Zhang, et al., Int J Coal Geol 195, 250–66 (2018)
6. T. Saif, Q. Lin, A.R. Butcher, B. Bijeljic, M.J. Blunt, Appl Energ 202, 628–47 (2017)
7. M. Akbarabadi, S. Saraji, M. Piri, D. Georgi, M. Delshad, Adv Water Resour 107, 160–79 (2017)
8. S. Chen, J. Jiang, B. Guo, Chem Eng J 417, 129210 (2021)
9. Y. Wu, P. Tahmasebi, C. Lin, L. Ren, C. Dong, Mar Petrol Geol 109, 9–21 (2019)
10. S. Kelly, H. El-Sobky, C. Torres-Verdín, M.T. Balhoff Adv Water Resour 95, 302–16 (2016)
11. M. Fleury, M. Romero-Sarmiento, J Petrol Sci Eng 137, 55–62 (2016)
12. P.M. Singer, Z. Chen, X. Wang, G.J. Hirasaki Fuel 280, 118626 (2020)
13. P.M. Singer, Z. Chen, G.J Hirasaki Petrophysics 57, 604–19 (2016)
14. R. Kausik, CC. Minh, L. Zielinski, B. Vissapragada, R. Akkurt, Y. Song, et al., SPE, SPE-147198-MS (2011)
15. R. Kausik, K. Fellah, L. Feng, G. Simpson, Petrophysics 58, 341–51 (2017)
16. R. Kausik, K. Fellah, E. Rylander, P.M. Singer, R.E. Lewis, S.M. Sinclair, Petrophysics 57, 339–50 (2016)
17. B. Sun, E. Yang, H. Wang, S.J. Seltzer, V. Montoya, J. Crowe, et al., SPWLA 57th Annual Logging Symposium (2016)
18. C. Minh, S. Crary, L. Zielinski, C.B. Liu, S. Jones, S. Jacobsen, SPE, SPE-161578-MS (2012)
19. Y-Q. Song, R. Kausik, Prog Nucl Mag Res Sp 112–113, 17–33 (2019)
20. R. Kausik, C.C Minh, L. Zielinski, B. Vissapragada, R. Akkurt, Y-Q. Song, et al., SPE, SPE-147198-MS (2011)
21. J-P. Korb, B. Nicot, I. Jolivet, Micropor Mesopor Mat 269, 7–11 (2018)
22. R. Enjilela, J. Guo, B. MacMillan, F. Marica, A. Afrough, B.J. Balcom, J Magn Reson 326, 106961 (2021)
23. J. Guo, B. MacMillan, M.S. Zamiri, B.J. Balcom, J Magn Reson 328, 107005 (2021)
24. M.S Zamiri, B. MacMillan, F. Marica, J. Guo, L. Romero-Zerón, B.J. Balcom, Fuel 284, 119014 (2021)
25. M.S. Zamiri, F. Marica, L. Romero-Zerón, B.J. Balcom, Chem Eng J 428, 131042 (2022)
26. J. Guo, M.S. Zamiri, B.J. Balcom, J Magn Reson 335, 107123 (2022)
27. B.J. Balcom, R.P. Macgregor, S.D. Beyea, D.P. Green, R.L. Armstrong, T.W Bremner, J Magn Reson A 123, 131–4 (1996)
28. M. Halse, D.J. Goodyear, B. MacMillan, P. Szomolanyi, D. Matheson, B.J Balcom, J Magn Reson 165, 219–29 (2003)
29. R. Kimmich, *NMR Tomography, Diffusometry, Relaxometry* (Springer Berlin Heidelberg; 1997)
30. P.T. Callaghan, *Translational Dynamics and Magnetic Resonance* (Oxford University Press, 2011)
31. J. Mitchell, J Magn Reason 240, 52–60 (2014)
32. I.V. Mastikhin, B.J. Balcom, P.J. Prado, C.B. Kennedy, J Magn Reson 136, 159–68 (1999)
33. L. Li, F. Marica, Q. Chen, B. MacMillan, B.J. Balcom, J Magn Reson 186, 282–92 (2007)
34. M. Labus, I. Matyasik, J Therm Anal Calorim 136, 1185–94 (2019)
35. B. Tissot, B. Durand, J. Espitalie, A. Combaz, AAPG Bull 58 (1974)